SHORT AND SPARSE DECONVOLUTION — A GEOMETRIC APPROACH

Anonymous authors
Paper under double-blind review

ABSTRACT

Short-and-sparse deconvolution (SaSD) is the problem of extracting localized, recurring motifs in signals with spatial or temporal structure. Variants of this problem arise in applications such as image deblurring, microscopy, neural spike sorting, and more. The problem is challenging in both theory and practice, as natural optimization formulations are nonconvex. Moreover, practical deconvolution problems involve smooth motifs (kernels) whose spectra decay rapidly, resulting in poor conditioning and numerical challenges. This paper is motivated by recent theoretical advances (Zhang et al., 2017; Kuo et al., 2019), which characterize the optimization landscape of a particular nonconvex formulation of SaSD. This is used to derive a *provable* algorithm which exactly solves certain non-practical instances of the SaSD problem. We leverage the key ideas from this theory (sphere constraints, data-driven initialization) to develop a *practical* algorithm, which performs well on data arising from a range of application areas. We highlight key additional challenges posed by the ill-conditioning of real SaSD problems, and suggest heuristics (acceleration, continuation, reweighting) to mitigate them. Experiments demonstrate the performance and generality of the proposed method.

1 INTRODUCTION

Many signals arising in science and engineering can be modeled as superpositions of basic, recurring motifs, which encode critical information about a physical process of interest. Signals of this type can be modeled as the convolution of a zero-padded short kernel $\boldsymbol{a}_0 \in \mathbb{R}^{p_0}$ (the motif) with a longer sparse signal $\boldsymbol{x}_0 \in \mathbb{R}^m$ ($m \gg p_0$) which encodes the locations of the motifs in the sample[1]:

$$\boldsymbol{y} = \iota \boldsymbol{a}_0 \circledast \boldsymbol{x}_0. \tag{1}$$

We term this a short-and-sparse (SaS) model. In practice, often only $\boldsymbol{y}$ is directly observed. *Short-and-sparse deconvolution* (SaSD) is the problem of recovering both $\boldsymbol{a}_0$ and $\boldsymbol{x}_0$ from $\boldsymbol{y}$. Variants of SaSD arise in areas such as microscopy (Cheung et al., 2018), astronomy (Briers et al., 2013), and neuroscience (Song et al., 2018). SaSD is a challenging inverse problem in both theory and practice. Natural formulations are nonconvex, and until recently very little algorithmic theory was available. Moreover, practical instances are typically ill-conditioned, due to the spectral decay of the kernel $\boldsymbol{a}_0$.

This paper is motivated by recent theoretical advances in nonconvex optimization and, in particular, on the geometry of SaSD. Zhang et al. (2017) and Kuo et al. (2019) study particular optimization formulations for SaSD and show that the landscape is largely driven by the *problem symmetries* of SaSD. They derive provable methods for idealized problem instances, which exactly recover $(\boldsymbol{a}_0, \boldsymbol{x}_0)$ up to trivial ambiguities. While inspiring, these methods are *not practical* and perform poorly on real problem instances. Where the emphasis of Zhang et al. (2017) and Kuo et al. (2019) is on theoretical guarantees, here we focus on practical computation. We show how to combine ideas from this theory with heuristics that better address the properties of practical deconvolution problems, to build a novel method that performs well on data arising in a range of application areas. A critical issue in moving from theory to practice is the poor conditioning of naturally-occurring deconvolution problems: we show how to address this with a combination of ideas from sparse optimization, such as momentum, continuation, and reweighting. The end result is a general purpose method, which we demonstrate on data from neural spike sorting, calcium imaging and fluorescence microscopy.

---

[1]For simplicity, (1) uses cyclic convolution; algorithms are results also apply to linear convolution with minor modifications. Here ι denotes the zero padding operator.

Notation. The zero-padding operator is denoted by $\iota : \mathbb{R}^p \to \mathbb{R}^m$. Projection of a vector $\boldsymbol{v} \in \mathbb{R}^p$ onto the sphere is denoted by $\mathcal{P}_{\mathbb{S}^{p-1}}(\boldsymbol{v}) \doteq \boldsymbol{v}/\|\boldsymbol{v}\|_2$, and $\mathcal{P}_{\boldsymbol{z}}(\boldsymbol{v}) \doteq \boldsymbol{v} - \langle \boldsymbol{v}, \boldsymbol{z} \rangle \boldsymbol{z}$ denotes projection onto the tangent space of $\boldsymbol{z} \in \mathbb{S}^{p-1}$. The Riemannian gradient of a function $f : \mathbb{S}^{p-1} \to \mathbb{R}$ at point $\boldsymbol{z}$ on the sphere is given by $\operatorname{grad} f(\boldsymbol{z}) \doteq \mathcal{P}_{\boldsymbol{z}}(\nabla f(\boldsymbol{z}))$.

2 SYMMETRY AND GEOMETRY IN SASD

An important observation of the SaSD problem is that it admits multiple equivalent solutions. This is purely due to the cyclic convolution between $\boldsymbol{a}_0$ and $\boldsymbol{x}_0$, which exhibits the trivial ambiguity[2]

$$\boldsymbol{y} \;=\; \iota \boldsymbol{a}_0 \circledast \boldsymbol{x}_0 \;=\; (\alpha s_\ell [\iota \boldsymbol{a}_0]) \;\circledast\; \left(\tfrac{1}{\alpha} s_{-\ell}[\boldsymbol{x}_0]\right),$$

for any nonzero scalar α and cyclic shift $s_\ell[\cdot]$. These scale and shift symmetries create several acceptable candidates for $\boldsymbol{a}_0$ and $\boldsymbol{x}_0$, and in the absence of further information we only expect to recover $\boldsymbol{a}_0$ and $\boldsymbol{x}_0$ up to symmetry. Furthermore, they largely drive the behavior of certain nonconvex optimization problems formulated for SaSD. Since the success of SaSD requires distinguishing between overlapping copies of $\boldsymbol{a}_0$, its difficulty also depends highly on the "similarity" of the $\boldsymbol{a}_0$ to its shifts. Here we capture this notion using the *shift-coherence* of $\boldsymbol{a}_0$,

$$\mu(\boldsymbol{a}_0) \;\doteq\; \max_{\ell \neq 0} |\langle \iota \boldsymbol{a}_0, s_\ell[\iota \boldsymbol{a}_0] \rangle| \;\in\; [0, 1]. \tag{2}$$

On the sphere, the shifts of $\boldsymbol{a}_0$ become closer together as $\mu(\boldsymbol{a}_0)$ increases, making objective landscapes for optimization less favorable for recovering any specific shift of $\boldsymbol{a}_0$.

2.1 LANDSCAPE GEOMETRY UNDER SHIFT-INCOHERENCE

A natural approach to solving SaSD is to formulate it as a suitable optimization problem. In this paper we will focus on the *Bilinear Lasso* (BL) problem, which minimizes the squared error between the observation $\boldsymbol{y}$ and its reconstruction $\boldsymbol{a} \circledast \boldsymbol{x}$, plus a ℓ_1-norm sparsity penalty on $\boldsymbol{x}$,

$$\min_{\boldsymbol{a} \in \mathbb{S}^{p-1}, \boldsymbol{x} \in \mathbb{R}^m} \left[\Psi_{\mathrm{BL}}(\boldsymbol{a}, \boldsymbol{x}) \;\doteq\; \tfrac{1}{2} \|\boldsymbol{y} - \iota \boldsymbol{a} \circledast \boldsymbol{x}\|_2^2 + \lambda \|\boldsymbol{x}\|_1 \right]. \tag{3}$$

Later in this section, we will see that the kernel length p should be set slightly larger than p_0.

The Bilinear Lasso is a nonconvex optimization problem, as the shift symmetries of SaSD create discrete local minimizers in the objective landscape. The regularization created by problem symmetries in nonconvex inverse problems are a fairly general phenomenon (Sun et al., 2015) and, as Kuo et al. (2019) shows, its influence in SaSD extends beyond the neighborhoods of these local minimizers. It analyzes an *Approximate Bilinear Lasso* (ABL) objective[3] Ψ_{ABL}, which satisfies

$$\Psi_{\mathrm{ABL}}(\boldsymbol{a}, \boldsymbol{x}) \simeq \Psi_{\mathrm{BL}}(\boldsymbol{a}, \boldsymbol{x}), \qquad \text{when } \mu(\boldsymbol{a}) \simeq 0.$$

This non-practical objective serves as a valid simplification of the Bilinear Lasso for analysis when the true kernel is itself incoherent, i.e. $\mu(\boldsymbol{a}_0) \simeq 0$ (Figures 1d and 1e). Under its marginalization[4]

$$\varphi_{\mathrm{ABL}}(\boldsymbol{a}) \;\doteq\; \min_{\boldsymbol{x} \in \mathbb{R}^m} \Psi_{\mathrm{ABL}}(\boldsymbol{a}, \boldsymbol{x}), \tag{4}$$

certain crucial properties regarding its curvature can be characterized for generic choices of $\boldsymbol{x}$, due to concentration of measure and reduction to a space of significantly smaller dimension $p \ll m$.

Curvature in the span of a few shifts. Suppose we set $p > p_0$, which ensures that we can find an $\boldsymbol{a} \simeq \alpha_1 s_{\ell_1}[\boldsymbol{a}_0] + \alpha_2 s_{\ell_2}[\boldsymbol{a}_0] \in \mathbb{S}^{p-1}$ that lies near the span of two shifts of $\boldsymbol{a}_0$. If $\alpha_1 \simeq \pm 1$ (or $\alpha_2 \simeq 0$) then, under suitable conditions on $\boldsymbol{a}_0$ and $\boldsymbol{x}_0$, Kuo et al. (2019) asserts that $\boldsymbol{a}$ lies in a strongly convex region of φ_{ABL}, containing a single minimizer near $s_{\ell_1}[\boldsymbol{a}_0]$ (Figure 1a); the converse is also true. A saddle-point exists nearby when $\alpha_1 \simeq \alpha_2$ is balanced, characterized by large negative curvature along the two shifts and positive curvature in orthogonal directions (Figure 1b). Interpolating between these two cases, large negative gradients point towards individual shifts.

---

[2]We therefore assume w.l.o.g. that $\|\boldsymbol{a}_0\|_2 = 1$ in this paper.

[3]As the intention here is apply some key intuition from the ABL objective towards the Bilinear Lasso itself, we intentionally omit the concrete form of $\Psi_{\mathrm{ABL}}(\boldsymbol{a})$. Readers may refer to Appendix A for more details.

[4]Minimizing φ_{ABL}, this is equivalent to minimizing Ψ_{ABL} as $\boldsymbol{x}$ can be recovered via convex optimization.
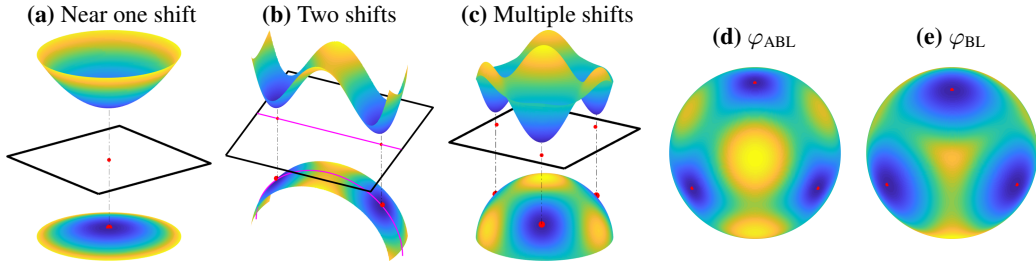
Figure 1: **Geometry of φ_{ABL} near superpositions of shifts** of a_0 (Kuo et al., 2019). **(a)** Regions near single shifts are strongly convex. **(b)** Regions between two shifts contain a saddle-point, with negative curvature towards each shift and positive curvature orthogonally. **(c)** The span of three shifts. **(d,e)** When $\mu_s(a_0) \approx 0$, the Bilinear Lasso $\varphi_{\text{BL}}(a) \doteq \min_x \Psi_{\text{BL}}(a, x)$ and ABL $\varphi_{\text{ABL}}(a)$ are empirically similar in the span of three shifts.

The behavior of φ_{ABL} between two shifts of a_0 — strong convexity near single shifts, and saddle-points near balanced points — extends to regions of the sphere spanned by several shifts (Figure 1c); we elaborate on this further in Appendix A.1. This regional landscape guarantees that a_0 can be efficiently recovered up to a signed shift using methods for first and second-order descent, as soon as a can be brought sufficiently close to the span of a few shifts.

Optimization over the sphere. For both the Bilinear Lasso and ABL, a unit-norm constraint on a is enforced to break the scaling symmetry between a_0 and x_0. Choosing the ℓ_2-norm, however, has surprisingly strong implications for optimization. The ABL objective, for example, is piecewise concave whenever a is sufficiently far away from any shift of a_0, but the sphere induces positive curvature near individual shifts to create strong convexity. These two properties combine to ensure recoverability of a_0. In contrast, enforcing ℓ_1-norm constraints often leads to spurious minimizers for deconvolution problems (Levin et al., 2011; Benichoux et al., 2013; Zhang et al., 2017).

Initializing near a few shifts. The landscape of φ_{ABL} makes single shifts of a_0 easy to locate if a is initialized near a span of a few shifts. Fortunately, this is a relatively simple matter in SaSD, as y is *itself a sparse superposition of shifts*. Therefore, one initialization strategy is to randomly choose a length-p_0 window $\widetilde{y}_i \doteq [y_i \ y_{i+1} \ldots y_{i+p_0-1}]^T$ from the observation and set

$$a^{(0)} \doteq \mathcal{P}_{\mathbb{S}^{p-1}}\left([\ \mathbf{0}_{p-1}\ ;\ \widetilde{y}_i\ ;\ \mathbf{0}_{p-1}\ ]\right). \tag{5}$$

This brings $a^{(0)}$ suitably close to the sum of a few shifts of a_0 (Appendix A.2); any truncation effects are absorbed by padding the ends of $\widetilde{y}_i$, which also sets the length for a to be $p = 3p_0 - 2$.

Implications for practical computation. The (regionally) benign optimization landscape of φ_{ABL} guarantees that efficient recovery is possible for SaSD when a_0 is incoherent. Applications of sparse deconvolution, however, are often motivated by sharpening or resolution tasks (Huang et al., 2009; Candès & Fernandez-Granda, 2014; Campisi & Egiazarian, 2016) where the motif a_0 is smooth and coherent (i.e. $\mu(a_0)$ is large). The ABL objective is a poor approximation of the Bilinear Lasso in such cases and fails to yield practical algorithms, so we should optimize the Bilinear Lasso directly.

From Figures 1d and 1e, we can see that low-dimensional subspheres spanned by shifts of a_0 are empirically similar when a_0 is incoherent. Although this breaks down in the coherent case, as we illustrate in Appendix A.3, the symmetry breaking properties of φ_{BL} remain present. This allows us to apply the geometric intuition discussed here to create an optimization method that, with the help of a number of computational heuristics, performs well in for SaSD even in general problem instances.

3 DESIGNING A PRACTICAL SaSD ALGORITHM

Several algorithms for SaSD-type problems have been developed for specific applications, such as image deblurring (Levin et al., 2011; Briers et al., 2013; Campisi & Egiazarian, 2016), neuroscience (Rey et al., 2015; Friedrich et al., 2017; Song et al., 2018), and image super-resolution (Baker &

Algorithm 1 Inertial Alternating Descent Method (iADM)

Input: Initializations $\boldsymbol{a}^{(0)} \in \mathbb{S}^{p-1}$, $\boldsymbol{x} \in \mathbb{R}^m$; observation $\boldsymbol{y} \in \mathbb{R}^m$; penalty $\lambda \geqslant 0$; momentum $\alpha \in [0, 1)$.
Output: $(\boldsymbol{a}^{(k)}, \boldsymbol{x}^{(k)})$, a local minimizer of Ψ_{BL}.
  Initialize $\boldsymbol{a}^{(1)} = \boldsymbol{a}^{(0)}$, $\boldsymbol{x}^{(1)} = \boldsymbol{x}^{(0)}$.
  for $k = 1, 2, \ldots$ until converged **do**
    Update $\boldsymbol{x}$ with accelerated proximal gradient step:

$$\boldsymbol{w}^{(k)} \leftarrow \boldsymbol{x}^{(k)} + \alpha \cdot \left(\boldsymbol{x}^{(k)} - \boldsymbol{x}^{(k-1)} \right)$$

$$\boldsymbol{x}^{(k+1)} \leftarrow \mathrm{soft}_{\lambda t_k} \left[\boldsymbol{w}^{(k)} - t_k \cdot \nabla_{\boldsymbol{x}} \psi_\lambda \left(\boldsymbol{a}^{(k)}, \boldsymbol{w}^{(k)} \right) \right],$$

    where $\mathrm{soft}_\lambda(\boldsymbol{v}) \doteq \mathrm{sign}(\boldsymbol{v}) \odot \max(|\boldsymbol{v} - \lambda|, \boldsymbol{0})$ denotes the soft-thresholding operator.
    Update $\boldsymbol{a}$ with accelerated Riemannian gradient step:

$$\boldsymbol{z}^{(k)} \leftarrow \mathcal{P}_{\mathbb{S}^{p-1}} \left(\boldsymbol{a}^{(k)} + \frac{\alpha}{\langle \boldsymbol{a}^{(k)}, \boldsymbol{a}^{(k-1)} \rangle} \cdot \mathcal{P}_{\boldsymbol{a}^{(k-1)}} \left(\boldsymbol{a}^{(k)} \right) \right)$$

$$\boldsymbol{a}^{(k+1)} \leftarrow \mathcal{P}_{\mathbb{S}^{p-1}} \left(\boldsymbol{z}^{(k)} - \tau_k \cdot \mathrm{grad}_{\boldsymbol{a}} \, \psi_\lambda \left(\boldsymbol{z}^{(k)}, \boldsymbol{x}^{(k+1)} \right) \right).$$
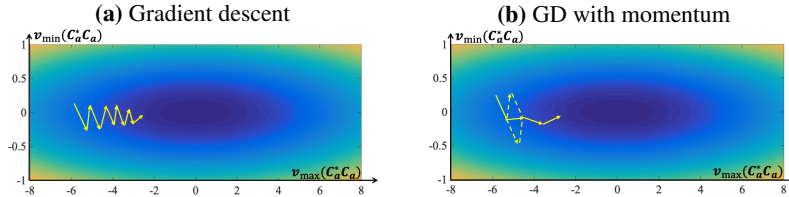
  end for

Figure 2: **Momentum acceleration.** a) Iterates of gradient descent oscillate on ill-conditioned functions; each marker denotes one iteration. b) Momentum dampens oscillation and speeds up convergence.

Kanade, 2002; Shtengel et al., 2009; Yang et al., 2010), or are augmented with additional structure (Wipf & Zhang, 2014; Ling & Strohmer, 2017; Walk et al., 2017).

Here, we instead leverage the theory from Section 2 to build an algorithm for general practical settings. In addition to applying an appropriate initialization scheme (5) and optimizing on the sphere, we minimize the Bilinear Lasso (3) instead of the ABL (4) to more accurately account for interactions between shifts of $\boldsymbol{a}_0$ in highly shift-coherent settings. Furthermore, we also address the negative effects of large coherence using a number of heuristics, leading to an efficient algorithm for SaSD.

Momentum acceleration. In shift-coherent settings, the Hessian of Ψ_{BL} becomes ill-conditioned near shifts of $\boldsymbol{a}_0$, a situation known to cause slow convergence for first-order methods (Nesterov, 2013). A remedy is to add momentum (Polyak, 1964; Beck & Teboulle, 2009) to first-order iterations, for instance, by augmenting gradient descent on some smooth $f(\boldsymbol{z})$ with stepsize τ with the term $\boldsymbol{w}$,

$$\boldsymbol{w}^{(k)} \leftarrow \boldsymbol{z}^{(k)} + \alpha \cdot \left(\boldsymbol{z}^{(k)} - \boldsymbol{z}^{(k-1)} \right) \tag{6}$$

$$\boldsymbol{z}^{(k+1)} \leftarrow \boldsymbol{w}^{(k)} - \tau \cdot \nabla f(\boldsymbol{w}^{(k)}). \tag{7}$$

Here, α controls the momentum added[5]. As illustrated in Figure 2, this additional term improves convergence by reducing oscillations of the iterates for ill-conditioned problems. Momentum has been shown to improve convergence for nonconvex and nonsmooth problems (Pock & Sabach, 2016; Jin et al., 2018). Here we provide an inertial alternating descent method (iADM) for finding local minimizers of Ψ_{BL} (Algorithm 1), which modifies iPALM (Pock & Sabach, 2016) to perform updates on $\boldsymbol{a}$ via retraction on the sphere (Absil et al., 2009)[6].

Homotopy continuation. It is also possible to improve optimization by modifying the objective Ψ_{BL} directly through the sparsity penalty λ. Variations of this idea appear in both Zhang et al. (2017) and Kuo et al. (2019), and can also help to mitigate the effects of large shift-coherence.

---

[5]Setting $\alpha = 0$ removes momentum and reverts to standard gradient descent.

[6]The stepsizes t_k and τ_k are obtained by backtracking (Nocedal & Wright, 2006; Pock & Sabach, 2016) to ensure sufficient decrease for $\Psi_{\mathrm{BL}}(\boldsymbol{a}^{(k)}, \boldsymbol{w}^{(k)}) - \Psi_{\mathrm{BL}}(\boldsymbol{a}^{(k)}, \boldsymbol{x}^{(k+1)})$, and vice versa.

Algorithm 2 SaS-BD with homotopy continuation

Input: Observation $\boldsymbol{y} \in \mathbb{R}^m$, motif size p_0; momentum $\alpha \in [0, 1)$; initial $\lambda^{(1)}$ final $\lambda^\star$, penalty decrease $\eta \in (0, 1)$; precision factor $\delta \in (0, 1)$.

Output: Solution path $\left\{ (\hat{\boldsymbol{a}}^{(n)}, \hat{\boldsymbol{x}}^{(n)}; \lambda^{(n)}) \right\}$ for SaSD.

 Set number of iterations $N \leftarrow \lfloor \log(\lambda^\star / \lambda^{(1)}) \,/\, \log \eta \rfloor$.

 Initialize $\hat{\boldsymbol{a}}^{(0)} \in \mathbb{R}^{3p_0 - 2}$ using (5), $\hat{\boldsymbol{x}}^{(0)} = \boldsymbol{0} \in \mathbb{R}^m$.

 for $n = 1, \dots, N$ **do**

  Minimize $\Psi_{\lambda^{(n)}}$ to precision $\delta \lambda^{(n)}$ with Algorithm 1:

$$\left(\hat{\boldsymbol{a}}^{(n)}, \hat{\boldsymbol{x}}^{(n)} \right) \leftarrow \mathrm{iADM}\left(\hat{\boldsymbol{a}}^{(n-1)}, \hat{\boldsymbol{x}}^{(n-1)}; \boldsymbol{y}, \lambda^{(n)}, \alpha \right).$$

  Update $\lambda^{(n+1)} \leftarrow \eta \lambda^{(n)}$.

 end for

(a) $\lambda = 5 \times 10^{-1}$	**(b)** $\lambda = 5 \times 10^{-2}$	**(c)** $\lambda = 5 \times 10^{-3}$
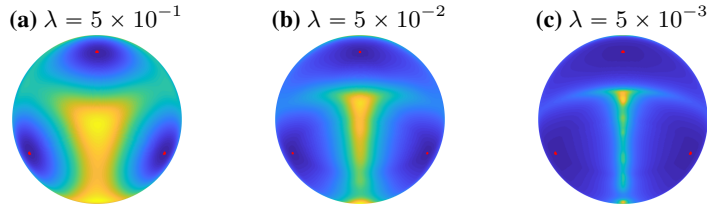
Figure 3: **Bilinear-lasso objective** φ_λ **on the sphere** $\mathbb{S}^{p-1}$, for $p = 3$ and varying λ; brighter colors indicate higher values. The function landscape of φ_λ flattens as sparse penalty λ decreases from left to right.

When solving (3) in the noise-free case, it is clear that larger choices of λ encourage sparser solutions for $\boldsymbol{x}$. Conversely, smaller choices of λ place local minimizers of the marginal objective $\varphi_{\mathrm{BL}}(\boldsymbol{a}) \doteq \min_{\boldsymbol{x}} \Psi_{\mathrm{BL}}(\boldsymbol{a}, \boldsymbol{x})$ closer to signed-shifts of $\boldsymbol{a}_0$ by emphasizing reconstruction quality. When $\mu(\boldsymbol{a}_0)$ is large, however, φ_{BL} becomes ill-conditioned as $\lambda \to 0$ due to the poor spectral conditioning of $\boldsymbol{a}_0$, leading to severe flatness near local minimizers and the creation spurious local minimizers when noise is present (Figure 3). Conversely, larger values of λ limit $\boldsymbol{x}$ to a small set of support patterns and simplify the landscape of φ_{BL}, at the expense of precision.

It is therefore important both for fast convergence and accurate recovery for λ to be chosen appropriately. When problem parameters — such as noise level, p_0, or θ — are not known a priori, a *homotopy continuation method* (Hale et al., 2008; Wright et al., 2009; Xiao & Zhang, 2013) can be used to obtain a range of solutions for SaSD. Using initialization (5), a rough estimate $(\hat{\boldsymbol{a}}^{(1)}, \hat{\boldsymbol{x}}^{(1)})$ is obtained by solving (3) with iADM using a large choice for $\lambda^{(1)}$. This estimate is refined via a *solution path* $\left\{ (\hat{\boldsymbol{a}}^{(n)}, \hat{\boldsymbol{x}}^{(n)}; \lambda^{(n)}) \right\}$ by gradually decreasing $\lambda^{(n)}$. By ensuring that $\boldsymbol{x}$ remains sparse along the solution path, the objective Ψ_{BL} enjoys restricted strong convexity w.r.t. both $\boldsymbol{a}$ and $\boldsymbol{x}$ throughout optimization (Agarwal et al., 2010). As a result, homotopy achieves linear convergence for SaSD where sublinear convergence is expected otherwise (Figures 4c and 4d). We provide a complete algorithm for SaSD combining Bilinear Lasso and homotopy continuation in Algorithm 2.

4   EXPERIMENTS

4.1   SYNTHETIC EXPERIMENTS

Here we perform SaSD in simulations on both coherent and incoherent settings. Coherent kernels are discretized from the Gaussian window function $\boldsymbol{a}_0 = \boldsymbol{g}_{n_0, 0.5}$, where $\boldsymbol{g}_{p, \sigma} \doteq \mathcal{P}_{\mathbb{S}^{p-1}}\left(\left[\exp\left(-\frac{(2i - p - 1)^2}{\sigma^2 (p-1)^2} \right) \right]_{i=1}^p \right)$. Incoherent kernels $\boldsymbol{a}_0 \sim \mathrm{Unif}(\mathbb{S}^{n_0 - 1})$ are sampled uniformly on the sphere.

Recovery performance.   We test recovery probability for varying kernel lengths n_0 and sparsity rates θ. To ensure the problem size is sufficiently large, we set $m = 100 n_0$. For each n_0 and θ, we randomly generate[7] $\boldsymbol{x} \sim_{\mathrm{i.i.d.}} \mathcal{BR}(\theta)$ for both coherent and incoherent $\boldsymbol{a}_0$. We solve ten trials of (3) on clean observation data $\boldsymbol{a}_0 \circledast \boldsymbol{x}_0$ using iADM with $\lambda = \frac{10^{-2}}{\sqrt{n_0 \theta}}$. The probability of recovering a signed

---

[7]$\mathcal{BR}(\theta)$ denotes the Bernoulli-Rademacher distribution, which has values ± 1 w.p. $\theta/2$ and zero w.p. $1 - \theta$.
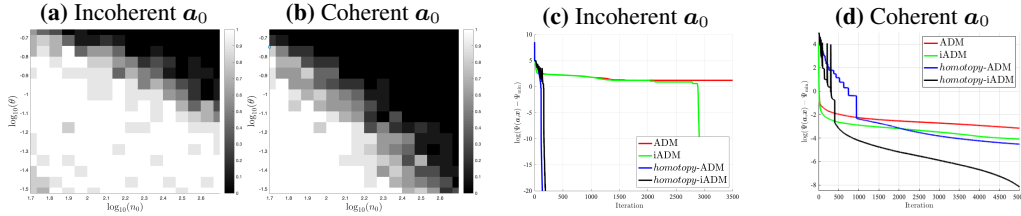
Figure 4: **Synthetic experiments for Bilinear Lasso.** *Success probability* (**a, b**): $x_0 \sim_{\text{i.i.d.}} \mathcal{BR}(\theta)$, the success probability of SaS-BD by solving (3), shown by increasing brightness, is large when the sparsity rate θ is sufficiently small compared to the length of a_0, and vice versa. Success with a fixed sparsity rate is more likely when a_0 is incoherent. *Algorithmic convergence* (**c, d**): convergence of function value for iADM with $\alpha_k = (k-1)/(k+1)$ vs. $\alpha_k = 0$ (ADM); with and without homotopy. Homotopy significantly improves convergence rate, and momentum improves convergence when a_0 is coherent.
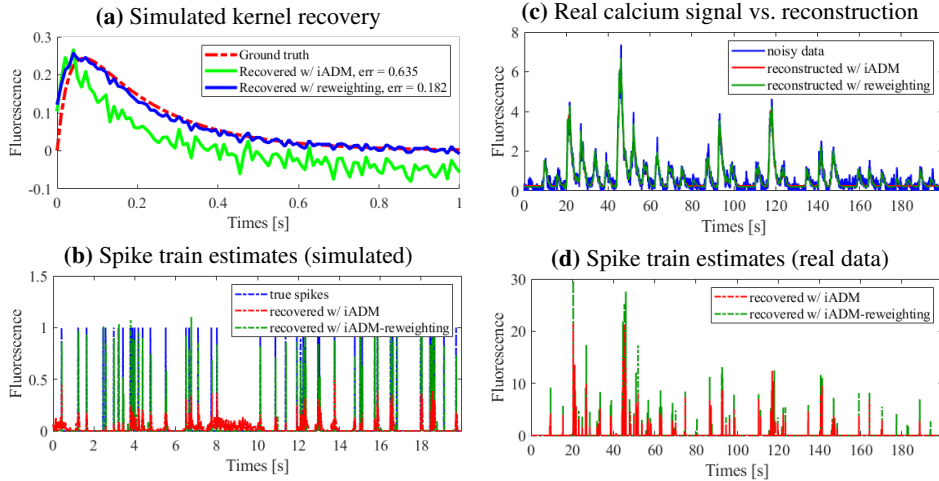

Figure 5: **Deconvolution for calcium imaging** using Algorithm 2 with iADM and with reweighting (Appendix B). *Simulated data:* (**a**) recovered AR2 kernel; (**b**) estimate of spike train. *Real data:* (**c**) reconstructed calcium signal (**d**) estimate of spike train. Reweighting improves estimation quality in each case.

shift of a_0 is shown in Figure 4. Recovery is likely when sparsity is low compared to the kernel length. The coherent problem setting has a smaller success region compared to the incoherent setting.

Momentum and homotopy. Next, we test the performance of Algorithm 1 with momentum ($\alpha_k = \frac{k-1}{k+2}$; see Pock & Sabach (2016)) and without ($\alpha = 0$). This is done by minimizing Ψ_{BL} with initialization (5), using clean observations with $n_0 = 10^2$, $m = 10^4$, and $\theta = n_0^{-3/4}$ for coherent and incoherent a_0. We also apply homotopy (Algorithm 2) with $\lambda^{(1)} = \max_\ell |\langle s_\ell[a^{(0)}], y \rangle|$ — see Xiao & Zhang (2013), $\lambda^\star = \frac{0.3}{\sqrt{n_0 \lambda}}$, $\eta = 0.8$, and $\delta = 0.1$. The final solve of (3) uses precision $\varepsilon^\star = 10^{-6}$, regardless of method. Figures 4c and 4d show the comparison results on coherent problem settings.

Comparison to existing methods. Finally, we compare iADM, and iADM with homotopy, against a number of existing methods for minimizing φ_{BL}. The first is *alternating minimization* (Kuo et al., 2019), which at each iteration k minimizes $a^{(k)}$ with $x^{(k)}$ fixed using accelerated (Riemannian) gradient descent with backtracking, and vice versa. The next method is the popular *alternating direction method of multipliers* (Boyd et al., 2011). Finally, we compare against iPALM (Pock & Sabach, 2016) with backtracking, using the unit ball constraint on a_0 instead of the unit sphere.

For each method, we deconvolve signals with $n_0 = 50$, $m = 100$, and $\theta = n_0^{-3/4}$ for both coherent and incoherent a_0. For both iADM, iADM with homotopy, and iPALM we set $\alpha = 0.3$. For homotopy, we set $\lambda^{(1)} = \max_\ell |\langle s_\ell[a^{(0)}], y \rangle|$, $\lambda^\star = \frac{0.3}{\sqrt{n_0 \lambda}}$, and $\delta = 0.5$. Furthermore we set $\eta = 0.5$ or $\eta = 0.8$ and for ADMM, we set the slack parameter to $\rho = 0.7$ or $\rho = 0.5$ for incoherent and coherent a_0 respectively. From Figure 6, we can see that ADMM performs better than iADM in the

6

incoherent case, but becomes less reliable in the coherent case. In both cases, iADM with homotopy is the best performer. Finally, we observe roughly equal performance between iPALM and iADM.
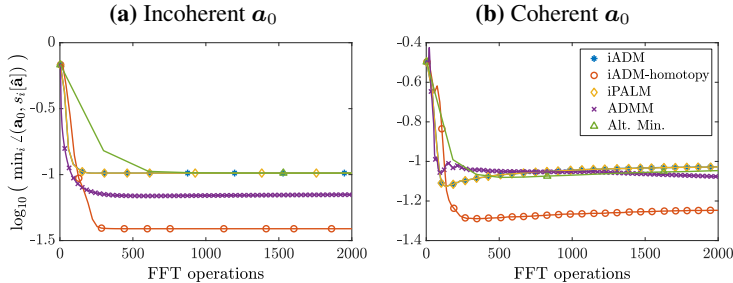

Figure 6: **Algorithmic comparison. (a)** Convergence of various methods minimizing Ψ_{BL} with incoherent $\boldsymbol{a}_0$ over FFT operations used (for computing convolutions). The y-axis denotes the log of the angle between $\boldsymbol{a}^{(k)}$ and the nearest shift of $\boldsymbol{a}_0$, and each marker denotes five iterations. **(b)** Convergence for coherent $\boldsymbol{a}_0$.

4.2 IMAGING APPLICATIONS

Here we demonstrate the performance and generality of the proposed method. We begin with calcium fluorescence imaging, a popular modality for studying spiking activity in large neuronal populations (Grienberger & Konnerth, 2012), followed by stochastic optical reconstruction microscopy (STORM) (Rust et al., 2006; Huang et al., 2008; 2010), a superresolution technique for *in vivo* microscopy[8].

Sparse deconvolution of calcium signals. Neural spike trains created by action potentials, each inducing a transient response in the calcium concentration of the surrounding environment. The aggregate signal can be modeled as a convolution between the transient $\boldsymbol{a}_0$ and the spike train $\boldsymbol{x}_0$. Whilst $\boldsymbol{a}_0$ nor $\boldsymbol{x}_0$ both encode valuable information, neither are perfectly known ahead of time.

Here, we first test our method on synthetic data generated using an AR2 model for $\boldsymbol{a}_0$, a shift-coherent kernel that is challenging for deconvolution, see e.g. Friedrich et al. (2017). We set $\boldsymbol{x}_0 \sim_{\text{i.i.d.}} \text{Bernoulli}(n_0^{-4/5}) \in \mathbb{R}^{10^4}$ with additive noise $\boldsymbol{n} \sim_{\text{i.i.d.}} \mathcal{N}(0, 5 \cdot 10^{-2})$. Figures 5a and 5b demonstrate accurate recovery of $\boldsymbol{a}_0$ and $\boldsymbol{x}_0$ in this synthetic setting. Next, we test our method on real data[9]; Figures 5c and 5d demonstrate recovery of spike locations. Although iADM provides decent performance, estimation quality can be improved by stronger sparsification methods, such as the reweighting technique by Candes et al. (2008), which we elaborate on in Appendix B.
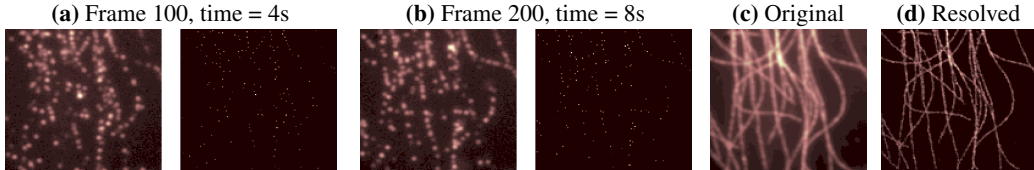

(a) Frame 100, time = 4s   **(b)** Frame 200, time = 8s   **(c)** Original   **(d)** Resolved

Figure 7: **SaSD for STORM imaging. (a, b)** Individual frames (left) and predicted point process map using SaSD (right). **(c, d)** shows the original microscopy and the super-resolved image obtained by our method.

Super-resolution for fluorescence microscopy. Fluorescence microscopy is often spatially limited by the diffraction of light; its wavelength (several hundred nanometers) is often larger than typical molecular length-scales in cells, preventing a detailed characterization of subcellular structures. The STORM technique overcomes this resolution limit by using photoswitchable fluorescent probes to multiplex the image into multiple frames, each containing a subset of the molecules present (Figure 7). If the location of these molecules can be precisely determined for each frame, synthesizing all deconvolved frames will produce a super-resolution microscopy image with nanoscale resolution.

---

[8]Other superresolution methods for microscopy include photoactivated localization microscopy (PALM) (Betzig et al., 2006), and fluorescence photoactivation localization microscopy (fPALM) (Hess et al., 2006).
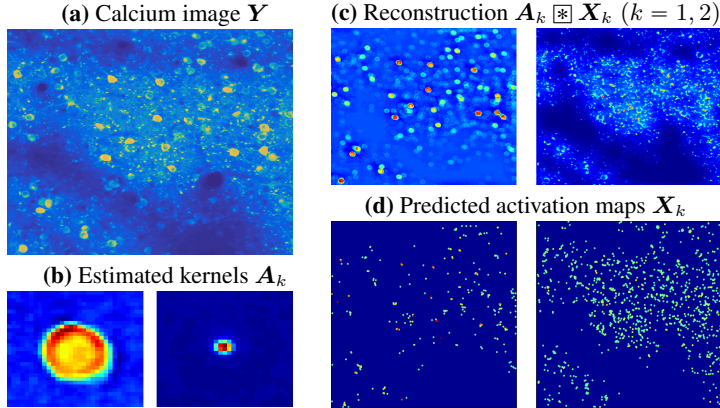
[9]Obtained at http://spikefinder.codeneuro.org.

(a) Calcium image $\boldsymbol{Y}$ **(c)** Reconstruction $\boldsymbol{A}_k \boxast \boldsymbol{X}_k$ $(k = 1, 2)$

(b) Estimated kernels $\boldsymbol{A}_k$ **(d)** Predicted activation maps $\boldsymbol{X}_k$

Figure 8: **Classification of calcium images. (a)** Original calcium image; **(b)** respective kernel estimates; **(c)** reconstructed images with the **(left)** neuron and **(right)** dendrite kernels; **(d)** respective occurence map estimates.

For each image frame, the localization task can be formulated via the SaS model

$$\underbrace{\boldsymbol{Y}_t}_{\text{STORM frame}} = \underbrace{\iota \boldsymbol{A}_0}_{\text{point spread function}} \boxast \underbrace{\boldsymbol{X}_{0,t}}_{\text{sparse point sources}} + \underbrace{\boldsymbol{N}_t}_{\text{noise}}. \tag{8}$$

Here we will solve this task on the single-molecule localization microscopy (SMLM) benchmarking dataset[10] via SaSD, recovering both the PSF $\boldsymbol{A}_0$ and the point source maps $\boldsymbol{X}_{0,t}$ simultaneously. We apply iADM with reweighting (Appendix B) on frames of size 128×128 from the video sequence "Tubulin"; each pixel is of 100nm^2 resolution[11], the fluorescence wavelength is 690nm, and the framerate is $f = 25$Hz. Figure 7 shows examples of recovered activation maps, and the aggregated super-resolution image from all 500 frames, accurately predicting the PSF (see Appendix D) and the activation map for each video frame to produce higher resolution microscopy images.

Localization in calcium images. Our methods are easily extended to handle superpositions of multiple SaS signals. In calcium imaging, this can potentially be used to track the neurons in video sequences, a challenging task due to (non-) rigid motion, overlapping sources, and irregular background noise Pnevmatikakis et al. (2016); Giovannucci et al. (2019). We consider frames video obtained via the two-photon calcium microscopy dataset from the Allen Institute for Brain Science[12], shown in Figure 8. Each frame contains the cross section of several neurons and dendrites, which have distinct sizes. We model this as the SaS signal $\boldsymbol{Y}_t = \iota \boldsymbol{A}_1 \boxast \boldsymbol{X}_{1,t} + \iota \boldsymbol{A}_2 \boxast \boldsymbol{X}_{2,t}$, where each summand consists of neurons or dendrites exclusively. By extending Algorithm 2 to recover each of the kernels $\boldsymbol{A}_k$ and maps $\boldsymbol{X}_k$, we can solve this *convolutional dictionary learning* (SaS-CDL; see Appendix C) problem which allows us to separate the dendritic and neuronal components from this image for localization of firing activity, etc. As a result, the application of SaS-CDL as a denoising or analysis tool for calcium imaging videos provides a very promising direction for future research.

5   DISCUSSION

Many nonconvex inverse problems, such as SaSD, are strongly regulated by their problem symmetries. Understanding this regularity and when or how it breaks down is important for developing effective algorithms. We illustrate this by combining geometric intuition with practical heuristics, motivated by common challenges in real deconvolution, to produce an efficient and general purpose method that performs well on data arising from a range of application areas. Our approach, therefore, can serve as a general baseline for studying and developing extensions to SaSD, such as SaS-CDL (Bristow & Lucey, 2014; Chun & Fessler, 2017; Garcia-Cardona & Wohlberg, 2018), Bayesian approaches (Babacan et al., 2008; Wipf & Zhang, 2014), and hierarchical SaS models (Chen et al., 2013).

---

[10]Data can be accessed at `http://bigwww.epfl.ch/smlm/datasets/index.html`.

[11]Here we solve SaSD on the same 128×128 grid. In practice, the localization problem is solved on a finer grid, so that the resulting resolution can reach $20 - 30$ nm.

[12]Obtained at `http://observatory.brain-map.org/visualcoding/`.

REFERENCES

Pierre-Antoine. Absil, Robert Mahoney, and Rodolphe Sepulchre. *Optimization Algorithms on Matrix Manifolds*. Princeton University Press, 2009.

Alekh Agarwal, Sahand Negahban, and Martin J Wainwright. Fast global convergence rates of gradient methods for high-dimensional statistical recovery. In *Advances in Neural Information Processing Systems*, pp. 37–45, 2010.

S Derin Babacan, Rafael Molina, and Aggelos K Katsaggelos. Variational bayesian blind deconvolution using a total variation prior. *IEEE Transactions on Image Processing*, 18(1):12–26, 2008.

Simon Baker and Takeo Kanade. Limits on super-resolution and how to break them. *IEEE Transactions on Pattern Analysis and Machine Intelligence*, 24(9):1167–1183, 2002.

Amir Beck and Marc Teboulle. A fast iterative shrinkage-thresholding algorithm for linear inverse problems. *SIAM Journal on Imaging Sciences*, 2(1):183–202, 2009.

Alexis Benichoux, Emmanuel Vincent, and Rémi Gribonval. A fundamental pitfall in blind deconvolution with sparse and shift-invariant priors. In *ICASSP-38th International Conference on Acoustics, Speech, and Signal Processing-2013*, 2013.

Eric Betzig, George H Patterson, Rachid Sougrat, O Wolf Lindwasser, Scott Olenych, Juan S Bonifacino, Michael W Davidson, Jennifer Lippincott-Schwartz, and Harald F Hess. Imaging intracellular fluorescent proteins at nanometer resolution. *Science*, 313(5793):1642–1645, 2006.

Stephen Boyd, Neal Parikh, Eric Chu, Borja Peleato, Jonathan Eckstein, et al. Distributed optimization and statistical learning via the alternating direction method of multipliers. *Foundations and Trends® in Machine learning*, 3(1):1–122, 2011.

David Briers, Donald D Duncan, Evan R Hirst, Sean J Kirkpatrick, Marcus Larsson, Wiendelt Steenbergen, Tomas Stromberg, and Oliver B Thompson. Laser speckle contrast imaging: theoretical and practical limitations. *Journal of biomedical optics*, 18(6):066018, 2013.

Hilton Bristow and Simon Lucey. Optimization methods for convolutional sparse coding. *arXiv preprint arXiv:1406.2407*, 2014.

Patrizio Campisi and Karen Egiazarian. *Blind image deconvolution: theory and applications*. CRC press, 2016.

Emmanuel J Candès and Carlos Fernandez-Granda. Towards a mathematical theory of super-resolution. *Communications on pure and applied Mathematics*, 67(6):906–956, 2014.

Emmanuel J Candes, Michael B Wakin, and Stephen P Boyd. Enhancing sparsity by reweighted ℓ_1 minimization. *Journal of Fourier analysis and applications*, 14(5-6):877–905, 2008.

Bo Chen, Gungor Polatkan, Guillermo Sapiro, David Blei, David Dunson, and Lawrence Carin. Deep learning with hierarchical convolutional factor analysis. *IEEE transactions on pattern analysis and machine intelligence*, 35(8):1887–1901, 2013.

Sky C Cheung, John Y Shin, Yenson Lau, Zhengyu Chen, Ju Sun, Yuqian Zhang, John N Wright, and Abhay N Pasupathy. Dictionary learning in fourier transform scanning tunneling spectroscopy. *arXiv preprint arXiv:1807.10752*, 2018.

Il Yong Chun and Jeffrey A Fessler. Convolutional dictionary learning: Acceleration and convergence. *IEEE Transactions on Image Processing*, 27(4):1697–1712, 2017.

Chaitanya Ekanadham, Daniel Tranchina, and Eero P Simoncelli. A blind sparse deconvolution method for neural spike identification. In *Advances in Neural Information Processing Systems*, pp. 1440–1448, 2011.

Johannes Friedrich, Pengcheng Zhou, and Liam Paninski. Fast online deconvolution of calcium imaging data. *PLoS Computational Biology*, 13(3):e1005423, 2017.

Cristina Garcia-Cardona and Brendt Wohlberg. Convolutional dictionary learning: A comparative review and new algorithms. *IEEE Transactions on Computational Imaging*, 4(3):366–381, 2018.

Andrea Giovannucci, Johannes Friedrich, Pat Gunn, Jeremie Kalfon, Brandon L Brown, Sue Ann Koay, Jiannis Taxidis, Farzaneh Najafi, Jeffrey L Gauthier, Pengcheng Zhou, et al. Caiman an open source tool for scalable calcium imaging data analysis. *Elife*, 8:e38173, 2019.

Christine Grienberger and Arthur Konnerth. Imaging calcium in neurons. *Neuron*, 73(5):862–885, 2012.

Elaine T Hale, Wotao Yin, and Yin Zhang. Fixed-point continuation for \ell_1-minimization: Methodology and convergence. *SIAM Journal on Optimization*, 19(3):1107–1130, 2008.

Samuel T Hess, Thanu PK Girirajan, and Michael D Mason. Ultra-high resolution imaging by fluorescence photoactivation localization microscopy. *Biophysical journal*, 91(11):4258–4272, 2006.

Bo Huang, Wenqin Wang, Mark Bates, and Xiaowei Zhuang. Three-dimensional super-resolution imaging by stochastic optical reconstruction microscopy. *Science*, 319(5864):810–813, 2008.

Bo Huang, Mark Bates, and Xiaowei Zhuang. Super-resolution fluorescence microscopy. *Annual Review of Biochemistry*, 78:993–1016, 2009.

Bo Huang, Hazen Babcock, and Xiaowei Zhuang. Breaking the diffraction barrier: super-resolution imaging of cells. *Cell*, 143(7):1047–1058, 2010.

Chi Jin, Rong Ge, Praneeth Netrapalli, Sham M Kakade, and Michael I Jordan. How to escape saddle points efficiently. In *Proceedings of the 34th International Conference on Machine Learning*, pp. 1724–1732, 2017.

Chi Jin, Praneeth Netrapalli, and Michael I Jordan. Accelerated gradient descent escapes saddle points faster than gradient descent. In *Conference On Learning Theory*, pp. 1042–1085, 2018.

Han-Wen Kuo, Yuqian Zhang, Yenson Lau, and John Wright. Geometry and symmetry in short-and-sparse deconvolution. In *International Conference on Machine Learning (ICML)*, June 2019.

Anat Levin, Yair Weiss, Fredo Durand, and William T Freeman. Understanding blind deconvolution algorithms. *IEEE Transactions on Pattern Analysis and Machine Intelligence*, 33(12):2354–2367, 2011.

Shuyang Ling and Thomas Strohmer. Blind deconvolution meets blind demixing: Algorithms and performance bounds. *IEEE Transactions on Information Theory*, 63(7):4497–4520, 2017.

Yurii Nesterov. *Introductory lectures on convex optimization: A basic course*, volume 87. Springer Science & Business Media, 2013.

Jorge Nocedal and Stephen Wright. *Numerical optimization*. Springer Science & Business Media, 2006.

Eftychios A Pnevmatikakis, Daniel Soudry, Yuanjun Gao, Timothy A Machado, Josh Merel, David Pfau, Thomas Reardon, Yu Mu, Clay Lacefield, Weijian Yang, et al. Simultaneous denoising, deconvolution, and demixing of calcium imaging data. *Neuron*, 89(2):285–299, 2016.

Thomas Pock and Shoham Sabach. Inertial proximal alternating linearized minimization (ipalm) for nonconvex and nonsmooth problems. *SIAM Journal on Imaging Sciences*, 9(4):1756–1787, 2016.

Boris T Polyak. Some methods of speeding up the convergence of iteration methods. *USSR Computational Mathematics and Mathematical Physics*, 4(5):1–17, 1964.

Hernan Gonzalo Rey, Carlos Pedreira, and Rodrigo Quian Quiroga. Past, present and future of spike sorting techniques. *Brain Research Bulletin*, 119:106–117, 2015.

Michael J Rust, Mark Bates, and Xiaowei Zhuang. Sub-diffraction-limit imaging by stochastic optical reconstruction microscopy (storm). *Nature Methods*, 3(10):793, 2006.

Gleb Shtengel, James A Galbraith, Catherine G Galbraith, Jennifer Lippincott-Schwartz, Jennifer M Gillette, Suliana Manley, Rachid Sougrat, Clare M Waterman, Pakorn Kanchanawong, Michael W Davidson, et al. Interferometric fluorescent super-resolution microscopy resolves 3d cellular ultrastructure. *Proceedings of the National Academy of Sciences*, 106(9):3125–3130, 2009.

Andrew H Song, Francisco Flores, and Demba Ba. Spike sorting by convolutional dictionary learning. *arXiv preprint arXiv:1806.01979*, 2018.

Ju Sun, Qing Qu, and John Wright. When are nonconvex problems not scary? *arXiv preprint arXiv:1510.06096*, 2015.

Philipp Walk, Peter Jung, Götz E Pfander, and Babak Hassibi. Blind deconvolution with additional autocorrelations via convex programs. *arXiv preprint arXiv:1701.04890*, 2017.

David Wipf and Haichao Zhang. Revisiting bayesian blind deconvolution. *The Journal of Machine Learning Research*, 15(1):3595–3634, 2014.

Stephen J Wright, Robert D Nowak, and Mário AT Figueiredo. Sparse reconstruction by separable approximation. *IEEE Transactions on Signal Processing*, 57(7):2479–2493, 2009.

Lin Xiao and Tong Zhang. A proximal-gradient homotopy method for the sparse least-squares problem. *SIAM Journal on Optimization*, 23(2):1062–1091, 2013.

Jianchao Yang, John Wright, Thomas S Huang, and Yi Ma. Image super-resolution via sparse representation. *IEEE Transactions on Image Processing*, 19(11):2861–2873, 2010.

Florence Yellin, Benjamin D Haeffele, and René Vidal. Blood cell detection and counting in holographic lens-free imaging by convolutional sparse dictionary learning and coding. In *IEEE 14th International Symposium on Biomedical Imaging*, pp. 650–653. IEEE, 2017.

Yuqian Zhang, Yenson Lau, Han-Wen Kuo, Sky Cheung, Abhay Pasupathy, and John Wright. On the global geometry of sphere-constrained sparse blind deconvolution. In *Computer Vision and Pattern Recognition (CVPR), 2017 IEEE Conference on*, pp. 4381–4389. IEEE, 2017.

Yin Zhou, Hang Chang, Kenneth Barner, Paul Spellman, and Bahram Parvin. Classification of histology sections via multispectral convolutional sparse coding. In *Proceedings of the IEEE Conference on Computer Vision and Pattern Recognition*, pp. 3081–3088, 2014.

A   APPROXIMATE BILINEAR LASSO OBJECTIVE

Recall from Section 2.2 of the main text that SaSD can be formulated as the Bilinear Lasso problem

$$\min_{\boldsymbol{a}\in\mathbb{S}^{p-1},\boldsymbol{x}\in\mathbb{R}^m} \left[\Psi_{\text{BL}}(\boldsymbol{a},\boldsymbol{x}) \;\doteq\; \tfrac{1}{2}\|\boldsymbol{y}-\iota\boldsymbol{a}\circledast\boldsymbol{x}\|_2^2 + \lambda\|\boldsymbol{x}\|_1 \right]. \tag{9}$$

Unfortunately, this objective is challenging for analysis. A major culprit is that its marginalization

$$\varphi_{\text{BL}}(\boldsymbol{a}) \;\doteq\; \min_{\boldsymbol{x}}\left\{ \tfrac{1}{2}\|\boldsymbol{y}-\iota\boldsymbol{a}\circledast\boldsymbol{x}\|_2^2 + \lambda\|\boldsymbol{x}\|_1 \right\}, \tag{10}$$

generally does not admit closed form solutions due the convolution with $\boldsymbol{a}$ in the squared error term. This motivates Kuo et al. (2019) to study the nonconvex formulation

$$\min_{\boldsymbol{a}\in\mathbb{S}^{p-1},\boldsymbol{x}\in\mathbb{R}^m} \left[\Psi_{\text{ABL}}(\boldsymbol{a},\boldsymbol{x}) \;\doteq\; \tfrac{1}{2}\|\boldsymbol{x}\|_2^2 - \langle\iota\boldsymbol{a}\circledast\boldsymbol{x},\boldsymbol{y}\rangle + \|\boldsymbol{y}\|_2^2 + \lambda\|\boldsymbol{x}\|_1 \right]. \tag{11}$$

We refer to (11) as the *Approximate Bilinear Lasso* formulation, and it is quite easy to see that $\Psi_{\text{ABL}}(\boldsymbol{a},\boldsymbol{x}) \approx \Psi_{\text{BL}}(\boldsymbol{a},\boldsymbol{x})$ when $\|\boldsymbol{a}\circledast\boldsymbol{x}\|^2 \approx \|\boldsymbol{x}\|^2$, i.e. if $\boldsymbol{a}$ is shift-incoherent, or $\mu(\boldsymbol{a}) \approx 0$. The marginalized objective function $\varphi_{\text{BL}}(\boldsymbol{a}) \;\doteq\; \min_{\boldsymbol{x}} \Psi_{\text{DQ}}(\boldsymbol{a},\boldsymbol{x})$ now has the closed form expression

$$\varphi_{\text{ABL}}(\boldsymbol{a}) \;\doteq\; -\tfrac{1}{2}\|\text{soft}_\lambda\left[\check{\boldsymbol{a}}\circledast\boldsymbol{y}\right]\|_2^2. \tag{12}$$

Here soft denotes the elementwise soft-thresholding operator $\text{soft}_t(x_i) = \text{sign}(x_i)\cdot\max(|x_i|-t,0)$, and $\check{\boldsymbol{a}}$ denotes the *adjoint kernel* of $\boldsymbol{a}$, i.e. the kernel s.t. $\langle\iota\boldsymbol{a}\circledast\boldsymbol{u},\boldsymbol{v}\rangle = \langle\boldsymbol{u},\check{\boldsymbol{a}}\circledast\boldsymbol{v}\rangle \;\forall\boldsymbol{u},\boldsymbol{v}\in\mathbb{R}^m$.

A.1 Landscape Geometry

The rest of Section 2.2 discusses the regional characterization of φ_{ABL} in the span of a small number of shifts from $\boldsymbol{a}_0$. This language is made precise in the form of the subsphere

$$\mathcal{S}_{\mathcal{I}} \doteq \left\{ \textstyle\sum_{\ell \in \mathcal{I}} \alpha_\ell s_\ell [\iota \boldsymbol{a}_0] \,:\, \alpha_\ell \in \mathbb{R} \right\} \bigcap \mathbb{S}^{p-1}, \tag{13}$$

spanned by a small set of cyclic shifts of $\iota \boldsymbol{a}_0$. Although we will not discuss the explicit distance function here, the characterization by Kuo et al. (2019) holds whenever $\boldsymbol{a}$ is close enough to such a subsphere with $|\mathcal{I}| \leqslant 4\theta p_0$, where θ is the probability that any individual entry of $\boldsymbol{x}_0$ is nonzero. Suppose we have $\boldsymbol{a} \approx \sum_{\ell \in \mathcal{I}} \alpha_\ell s_\ell [\iota \boldsymbol{a}_0]$ for some appropriate index set $\mathcal{I}$. Note that if $\mu_s \boldsymbol{a}_0 \approx 0$, then $\mu_s \boldsymbol{a} \approx 0$, $\forall \boldsymbol{a} \in \mathcal{S}_{\mathcal{I}}$. Now let $\alpha_{(1)}$ and $\alpha_{(2)}$ be the first and second largest coordinates of the shifts participating in $\boldsymbol{a}$, and let $s_{(1)}[\boldsymbol{a}_0]$ and $s_{(2)}[\boldsymbol{a}_0]$ be the corresponding shifts. Then

- If $\left| \frac{\alpha_{(2)}}{\alpha_{(1)}} \right| \approx 0$, then $\boldsymbol{a}$ is in a strongly convex region of φ_{ABL}, containing a *single* local minimizer corresponding to $s_{(1)}[\boldsymbol{a}_0]$.

- If $\left| \frac{\alpha_{(2)}}{\alpha_{(1)}} \right| \approx 1$, then $\boldsymbol{a}$ is near a saddle-point, with *negative curvature* pointing towards $s_{(1)}[\boldsymbol{a}_0]$ and $s_{(2)}[\boldsymbol{a}_0]$. If $\left| \frac{\alpha_{(3)}}{\alpha_{(2)}} \right| \approx 0$, i.e. $s_{(1)}[\boldsymbol{a}_0]$ and $s_{(2)}[\boldsymbol{a}_0]$ are the only two participating shifts, then φ_{ABL} is also characterized by *positive curvature* in all orthogonal directions.

- Otherwise, $\langle -\text{grad}\varphi_{\text{ABL}}(\boldsymbol{a}), \boldsymbol{z} - a \rangle$ takes on a *large positive value*, for either $u = s_{(1)}[\boldsymbol{a}_0]$ or $u = s_{(2)}[\boldsymbol{a}_0]$, i.e. the negative Riemannian gradient is large and points towards one of the participating shifts.

This is an example of a *ridable saddle* property (Jin et al., 2017) that allows many first and second-order methods to locate local minimizers. Since all local minimizers of φ_{ABL} near $\mathcal{S}_{\mathcal{I}}$ must correspond to signed-shifts of $\boldsymbol{a}_0$, this guarantees that the Approximate Bilinear Lasso formulation can be efficiently solved to recover $\boldsymbol{a}_0$ (and subsequently $\boldsymbol{x}_0$) for incoherent $\boldsymbol{a}_0$, as long as $\boldsymbol{a}$ is initialized near some appropriate subsphere and the sparsity coherence tradeoff $p_0 \theta \lessgtr (\mu_s(\boldsymbol{a}_0))^{-1/2}$ is satisfied. We note that this is a poor tradeoff rate, which reflects that the Approximate Bilinear Lasso formulation is non-practical and cannot handle SaSD problems involving kernels with high shift-coherence.

A.2 Data-driven initialization

For the SaS-BD problem, we usually initialize $\boldsymbol{x}$ by $\boldsymbol{x}^{(0)} = \boldsymbol{0}$, so that our initialization is sparse. For the optimization variable $\boldsymbol{a} \in \mathbb{R}^n$, recall from Section 2.2 in the main text that it is desirable to obtain an initialization $\boldsymbol{a}^0$ which is close to the intersection of $\mathbb{S}^{p-1}$ and a subsphere $\mathcal{S}_{\mathcal{I}}$ spanned by a few shifts of $\boldsymbol{a}_0$. When $\boldsymbol{x}_0$ is sparse, our measurement $\boldsymbol{y}$ is a linear combination of a few shifts of $\boldsymbol{a}_0$. Therefore, an arbitrary consecutive p_0-length window $\tilde{\boldsymbol{y}}_i \doteq [y_i \ y_{i+1} \ldots y_{i+p_0-1}]^T$ of the data $\boldsymbol{y}$ should be not far away from such a subspace $\mathcal{S}_{\mathcal{I}}$. As illustrated in Figure 9, one step of the generalized power method (Kuo et al., 2019)

$$\tilde{\boldsymbol{a}}^{(0)} \doteq \mathcal{P}_{\mathbb{S}^{p-1}}\big([\, \boldsymbol{0}_{p-1} \,;\, \tilde{\boldsymbol{y}}_i \,;\, \boldsymbol{0}_{p-1} \,] \big) \tag{14}$$

$$\boldsymbol{a}^{(0)} = \mathcal{P}_{\mathbb{S}^{n-1}}\left(-\nabla\varphi_{\text{ABL}}\left(\tilde{\boldsymbol{a}}^{(0)} \right) \right) \tag{15}$$

produces a refined initialization that is very close to a subspace $\mathcal{S}_{\mathcal{I}}$ spanned by a few shifts of $\boldsymbol{a}_0$ with $|\mathcal{I}| \approx \theta p_0$. However, (15) is a relatively complicated for a simple idea. In practice, we find that the simple initialization $\boldsymbol{a}^{(0)} = \tilde{\boldsymbol{a}}^{(0)}$ from (14) works suitably well for solving SaSD with (9).

A.3 Comparison to the Bilinear Lasso

Although it is easy to see that $\Psi_{\text{ABL}}(\boldsymbol{a})$ and $\Psi_{\text{BL}}(\boldsymbol{a})$ are similar as long as $\mu(\boldsymbol{a}) \approx 0$, it is also clear that these two quantities can be very different when $\mu(\boldsymbol{a})$ is large. This is especially significant when $\mu(\boldsymbol{a}_0)$ is itself large, as the desired solutions for $\boldsymbol{a}$ are then also coherent.

From Figure 10, we can see that these changes are reflected in the low-dimensional subspheres (13) spanned by adjacent shifts of $\boldsymbol{a}_0$. Compared to the incoherent case, φ_{BL} also takes on small values in
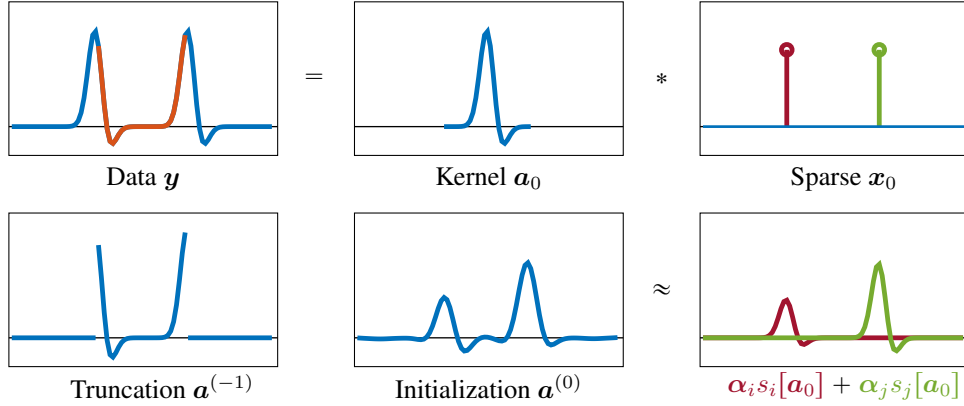
Figure 9: **Data-driven initialization for a:** using a piece of the observed data y to generate a good initial point $a^{(0)}$. **Top**: data $y = a_0 \circledast x_0$ is a superposition of shifts of the true kernel a_0. **Bottom**: a length-p_0 window contains pieces of just a few shifts. *Bottom-center*: one step of the generalized power method approximately fills in the missing pieces, yielding an initialization that is close to a linear combination of shifts of a_0 (*right*).
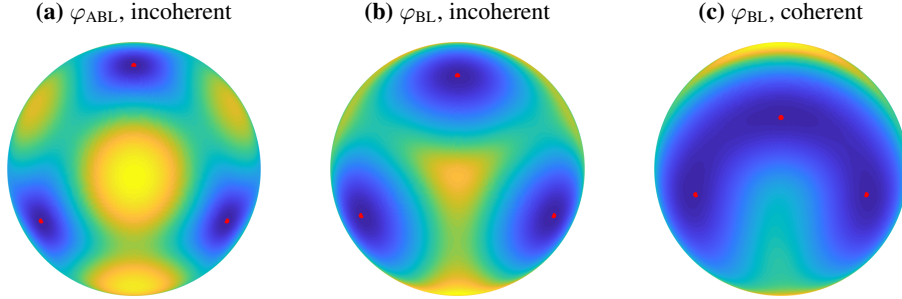
Figure 10: **Low-dimensional subspheres** spanned by shifts of a_0. Subfigures **(a,b)** present the optimization landscapes of $\varphi_{\mathrm{ABL}}(a)$ and $\varphi_{\mathrm{BL}}(a)$, for $a \in \mathbb{S}^{p-1} \bigcap \mathrm{span}\{a_0, s_1[a_0], s_2[a_0]\}$, with higher values being brighter. The red dots denote the shifts of a_0. Subfigure **(c)** shows the landscape φ_{BL} when a_0 is coherent, which significantly departs from the landscapes of **(a,b)**, but still retains symmetry breaking curvature.

regions between adjacent shifts, creating a "global valley" on the subsphere. Theoretically, this makes it difficult to ensure exact recovery of up to symmetry when a_0 is coherent, and the objective function becomes much more complicated. This is not a significant issue in terms of practical computation, however, since adjacent shifts of a_0 become indistinguishable as $\mu(a_0) \to 1$, meaning that one only needs to ensure that a lands in the "global valley" to achieve good estimates of a_0 up to symmetry.

B   REWEIGHTED SPARSE PENALIZATION

When a_0 is shift-coherent, minimization of the objective Ψ_{BL} with respect to x becomes sensitive to perturbations, creating "smudging" effects on the recovered map x. These resolution issues can be remedied with stronger *concave* regularizers. A simple way of facilitating this with the Bilinear Lasso is to use a reweighting technique (Candes et al., 2008). The basic idea is to adaptively adjust the penalty by considering a weighted variant of the original Bilinear Lasso problem from (9),

$$\min_{a \in \mathbb{S}^{p-1}, x \in \mathbb{R}^m} \quad \Psi_{\mathrm{BL}}^w(a, x) \doteq \tfrac{1}{2} \|y - a \circledast x\|_2^2 + \lambda \|w \odot x\|_1 \tag{16}$$

where $w \in \mathbb{R}_+^m$ and $\odot$ denotes the Hadamard product. Here we will set the weights w to be roughly inverse to the magnitude of the true signal x_0, i.e.,

$$w_i = \frac{1}{|x_{0,i}| + \varepsilon}. \tag{17}$$

In addition to choosing $\lambda > 0$, here $\varepsilon > 0$ trades off between sparsification strength (small ε) and algorithmic stability (large ε). Let $|x|_{(i)}$ denote the i-th largest entry of $|x|$. For experiments in the

---

Algorithm 3 Reweighted Bilinear Lasso

Input: Initializations $\hat{\boldsymbol{a}}^{(0)}, \hat{\boldsymbol{x}}^{(0)}$, penalty $\lambda > 0$
Output: Local minimizers $\hat{\boldsymbol{a}}^{(j)}, \hat{\boldsymbol{x}}^{(j)}$ of $\Psi_{\mathrm{BL}}^{\boldsymbol{w}^{(j)}}$.
  Initialize $\boldsymbol{w}^{(1)} = \boldsymbol{1}_m, j \leftarrow 1$.
  while not converged **do**
    Using the initialization $\left(\hat{\boldsymbol{a}}^{(j-1)}, \hat{\boldsymbol{x}}^{(j-1)} \right)$ and weight $\boldsymbol{w}^{(j)}$, solve (16) — e.g. with iADM — to obtain solution $\left(\hat{\boldsymbol{a}}^{(j)}, \hat{\boldsymbol{x}}^{(j)} \right)$;
    Set ε with (19) and update the weights as

$$\boldsymbol{w}^{(j+1)} \;=\; \frac{1}{\left| \hat{\boldsymbol{x}}^{(j)} \right| + \varepsilon}. \tag{18}$$

    Update $\ell \leftarrow \ell + 1$.
  end while

(a) True map $\boldsymbol{x}_0$ **(c)** Noisy $\boldsymbol{y}$, ℓ_1 only   **(e)** Noisy $\boldsymbol{y}$, reweighted

(b) True motif $\boldsymbol{a}_0$ **(d)** Noisy $\boldsymbol{a}$, ℓ_1 only   **(f)** Noisy $\boldsymbol{a}$, reweighted
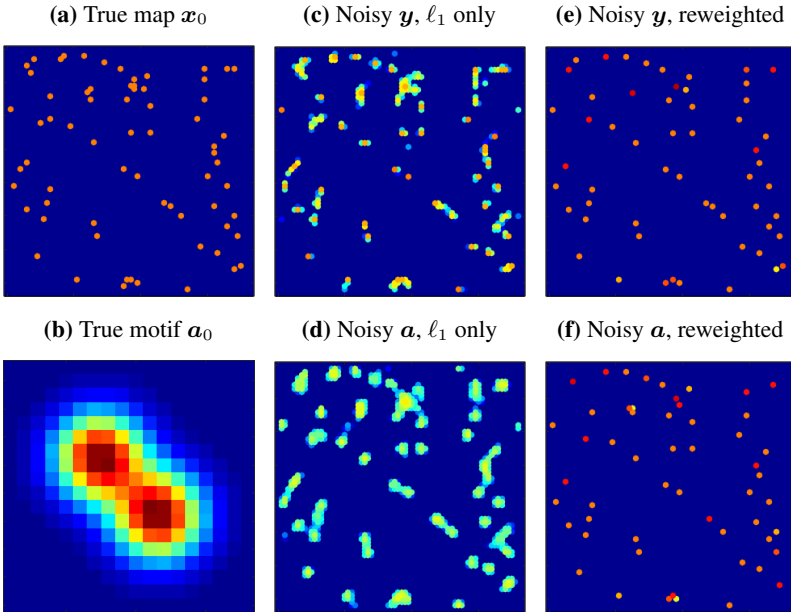
Figure 11: **Recovery of $\boldsymbol{x}_0$ with ℓ_1-reweighting. (a, b)** Truth signals. **(c)** Solving $\min_{\boldsymbol{x}} \Psi_{\mathrm{BL}}(\boldsymbol{a}, \boldsymbol{x})$ with noisy data and coherent $\boldsymbol{a}_0$ leads to low-quality estimates of $\boldsymbol{x}$; **(d)** performance suffers further when $\boldsymbol{a}$ is a noisy estimate of $\boldsymbol{a}_0$. **(e, f)** Reweighted ℓ_1 minimization alleviates this issue significantly.

main text, we set

$$\varepsilon = \max \left\{ |x|_{(\lceil n/\log(m/n) \rceil)} , 10^{-3} \right\}. \tag{19}$$

Starting with the initial weights $\boldsymbol{w}^{(0)} = \boldsymbol{1}_m$, Algorithm 3 successively solves (16), updating the weights using (17) at each outer loop iteration j. As $j \to \infty$, this method becomes equivalent to replacing the ℓ_1-norm in (9) with the nonconvex penalty $\sum_i \log(|x_i| + \varepsilon)$ (Candes et al., 2008).

We can easily adopt our iADM algorithm to solve this subproblem, by taking the proximal gradient on x with a different penalty λ_i for each entry x_i. Figure 11, as well as calcium imaging experiments in Section 4.2, Figure 5 of the main text, demonstrate improved estimation as a result of this method.

C   EXTENSION FOR CONVOLUTIONAL DICTIONARY LEARNING

The optimization methods we introduced for SaSD here can be naturally extended for sparse blind deconvolution problems with multiple kernels/motifs (a.k.a. convolutional dictionary learning; see Garcia-Cardona & Wohlberg (2018)), which have broad applications in microscopy data analysis
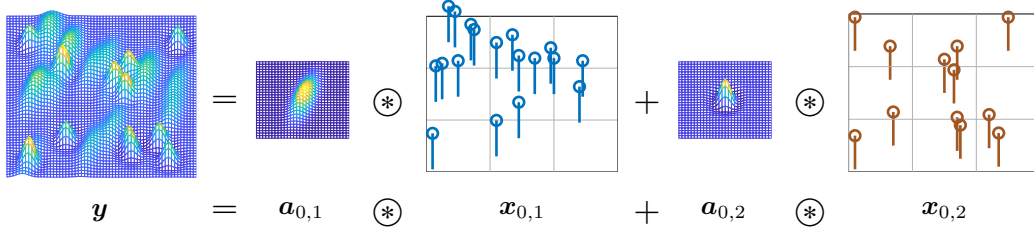
Figure 12: **Convolutional dictionary learning.** Simultaneous recovery for multiple unknown kernels $\{a_{0,k}\}_{k=1}^{N}$ and sparse activation maps $\{x_{0,k}\}_{k=1}^{N}$ from $y = \sum_{k=1}^{N} a_{0,k} \circledast x_{0,k}$.
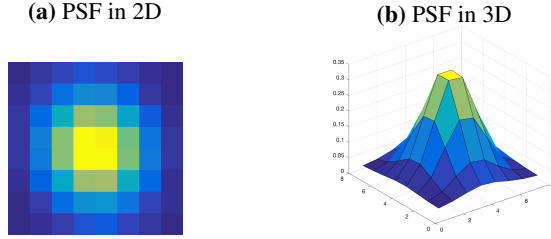
(a) PSF in 2D

(b) PSF in 3D

Figure 13: **Estimated PSF for STORM imaging.** The left hand side shows the estimated 8×8 PSF in 2D, the right hand side visualizes the PSF in 3D.

(Yellin et al., 2017; Zhou et al., 2014; Cheung et al., 2018) and neural spike sorting (Ekanadham et al., 2011; Rey et al., 2015; Song et al., 2018). As illustrated in Figure 12, the new observation y is the sum of N convolutions between short kernels $\{a_{0,k}\}_{k=1}^{N}$ and sparse maps $\{x_{0,k}\}_{k=1}^{N}$,

$$ y = \sum_{k=1}^{N} \iota a_{0,k} \circledast x_{0,k}, \qquad a_{0,k} \in \mathbb{R}^{p_0}, \quad x_{0,k} \in \mathbb{R}^{m}, \quad (1 \leqslant k \leqslant N). \qquad (20) $$

The natural extension of SaSD, then, is to recover $\{a_{0,k}\}_{k=1}^{N}$ and $\{x_{0,k}\}_{k=1}^{N}$ up to signed, shift, and permutation ambiguities, leading to the SaS convolutional dictionary learning (SaS-CDL) problem. The SaSD problem can be seen as a special case of SaS-CDL with $N = 1$. Based on the Bilinear Lasso formulation in (9) for solving SaSD, we constrain all kernels $a_{0,k}$ over the sphere, and consider the following nonconvex objective:

$$ \min_{\{a_k\}_{k=1}^{N}, \{x_k\}_{k=1}^{N}} \frac{1}{2} \left\| y - \sum_{k=1}^{N} a_k \circledast x_k \right\|_2^2 + \lambda \sum_{k=1}^{N} \|x_k\|_1, \quad \text{s.t.} \quad a_k \in \mathbb{S}^{p-1} \quad (1 \leqslant k \leqslant N). \quad (21) $$

Similar to the idea of solving the Bilinear Lasso in (9), we optimize (21) via iADM, by taking alternating descent steps on $\{a_k\}_{k=1}^{N}$ and $\{x_k\}_{k=1}^{N}$ with the other variable fixed.

D   SUPER-RESOLUTION WITH STORM IMAGING

For point source localization in STORM frames, recall that we use the SaS model from Section 4.2.2,

$$ \underbrace{Y_t}_{\text{STORM frame}} = \underbrace{\iota A_0}_{\text{point spread function}} \boxed{\circledast} \underbrace{X_{0,t}}_{\text{sparse point sources}} + \underbrace{N_t}_{\text{noise}}. \qquad (22) $$

We then apply our SaSD method to recover both A_0 and $X_{0,t}$ from Y_t. We show our recovery of $X_{0,t}$ as well as the super-resolved image using all available frames in Figure 6 of the main text. Since the main objective of STORM imaging is to recover the point sources, we have deferred the recovered PSF A_0 to Figure 13 here.